



# Achieving room temperature hydrogen storage reversibility in Nb-rich alloys of the Nb-Cr-Mn system



Bruno Hessel Silva <sup>a,b,\*</sup>, Walter José Botta <sup>a,c</sup>, Guilherme Zepon <sup>a,c</sup>

<sup>a</sup> Federal University of São Carlos, Department of Materials Engineering (DEMa/UFSCar), Rod. Washington Luiz, km 235, São Carlos, São Paulo CEP:13565-905, Brazil

<sup>b</sup> Department of Technology Systems, University of Oslo, Gunnar Randers vei 19, Kjeller 2027, Norway

<sup>c</sup> Federal University of São Carlos, Graduate Program in Materials Science and Engineering (PPGCEM/UFSCar), Rod. Washington Luiz, km 235, São Carlos, São Paulo CEP:13565-905, Brazil

## ARTICLE INFO

### Keywords:

Metal hydrides  
CALPHAD  
Multi-phase alloys  
Hydrogen storage

## ABSTRACT

Recent developments in the design of body-centered cubic (BCC) multicomponent alloys via computational tools have demonstrated the possibility of obtaining alloys with excellent hydrogen storage behavior. In this work, we employ the CALPHAD (Calculation of Phase Diagrams) method to design Nb-rich alloys of the Nb-Cr-Mn system that present hydrogen storage reversibility at room temperature under moderate pressure conditions. We employ the valence electron concentration (VEC) factor as a compositional guide to select compositions with suitable thermodynamic properties. Using electric arc melting, we synthesize two alloys, namely Nb<sub>85</sub>Cr<sub>10</sub>Mn<sub>5</sub> and Nb<sub>70</sub>Cr<sub>20</sub>Mn<sub>10</sub>, both forming predominant BCC solid solutions with VEC ~ 5.2 and minor amounts of a eutectic microconstituent composed of BCC and Laves C14 phases. Both alloys are easily hydrogenated at room temperature without the need for an activation treatment. The Nb<sub>85</sub>Cr<sub>10</sub>Mn<sub>5</sub> alloy reaches a storage capacity of 2.1 wt% of H (298 K; P<sub>eq</sub> ~ 20 bar) whereas the Nb<sub>70</sub>Cr<sub>20</sub>Mn<sub>10</sub> alloy reaches a capacity of 1.4 wt% (298 K; P<sub>eq</sub> ~ 21 bar). Benefits in the storage kinetic performance are correlated with the BCC + C14 microstructure. Pressure-Composition-Temperature (PCT) diagrams show moderate values of equilibrium pressure for hydrogen storage reversibility at room temperature. Room temperature absorption/desorption cycling measurements demonstrated a reversible capacity of 1.2 wt% of H (P<sub>eq</sub> ~ 29 bar) for the Nb<sub>85</sub>Cr<sub>10</sub>Mn<sub>5</sub> alloy and 0.8 wt% of H (P<sub>eq</sub> ~ 31 bar) for the Nb<sub>70</sub>Cr<sub>20</sub>Mn<sub>10</sub> alloy after twenty cycles.

## 1. Introduction

With the rise of low carbon emission hydrogen as an energy carrier, metal hydrides might play a crucial role in hydrogen storage applications [1]. Metal hydrides provide high-density hydrogen storage, and they have the potential to be applied in both mobile and stationary applications such as tanks and compressors [1,2]. In this context, multicomponent alloy systems have gained the attention of several research groups due to their excellent hydrogen storage properties, including rapid hydrogen absorption/desorption reactions, easy activation, and hydrogen storage reversibility at moderate pressure and temperature [3]. An attractive feature of these alloys is the wide number of possible systems and compositions, which offers the opportunity to tailor specific hydrogen storage properties through chemical compositional control [4,5]. For instance, Strozi et al. [6,7] showed the possibility of increasing the hydrogen absorption/desorption equilibrium

pressure in Ti-V-Nb-Cr BCC alloys by adjusting the Cr/(TiVNb) ratio. Similarly, Silva et al. [8] used thermodynamic modeling to design Ti-V-Nb-Cr alloys for room temperature hydrogen storage reversibility. The authors found a BCC composition (Ti<sub>11</sub>V<sub>30</sub>Nb<sub>28</sub>Cr<sub>31</sub>) that presented 1.7 wt% of hydrogen reversible capacity at room temperature. Remarkably, in both studies, the alloys were easily hydrogenated without the need for an activation treatment, and they were fully hydrogenated in a few minutes at room temperature.

Within this context, different strategies have been reported on how to design multicomponent alloys for hydrogen storage. Researchers have employed semi-empirical and empirical structural factors as guiding principles to find potential systems/compositions for hydrogen storage applications [3,9–11]. For example, many authors [5,10,12] reported correlations of hydrogen storage properties with the valence electron concentration (VEC) factor, which is given by Eq. (1):

\* Corresponding author at: Department of Technology Systems, University of Oslo, Gunnar Randers vei 19, Kjeller 2027, Norway.

E-mail address: [b.h.silva@its.uio.no](mailto:b.h.silva@its.uio.no) (B.H. Silva).

$$VEC = \sum_{i=1}^N \{c_i(VEC)_i\} \quad (1)$$

where  $c_i$  and  $(VEC)_i$  are the atomic fraction and the VEC of each element in the alloy composition, respectively. Nygård et al. [10] claimed that multicomponent alloys with high VEC values ( $VEC > 5.0$ ) displayed reduced storage capacities due to hydride destabilization. Likewise, Somo et al. [5] reported proportional correlations between VEC values of multicomponent alloys and their hydrogen storage capacity. Silva et al. [12] suggested a correlation between VEC and the thermodynamic properties for hydrogenation of Ti-V-Nb-M (M = Co, Cr, and Ni) alloys. The authors highlighted the obtention of similar enthalpy and entropy values for FCC hydride formation and decomposition in BCC multicomponent alloys with the same VEC values.

Furthermore, many authors have also been using computational thermodynamic tools to design multicomponent alloys for hydrogen storage [7,8,12–17]. For example, the CALPHAD method has been widely used to predict the phase stability of compositions that are prone to form BCC alloys and/or intermetallics such as Laves C14 [3,7,8,12, 16–18]. This computational method has highlighted another important aspect of multicomponent systems: the flexibility in achieving: i) single-phase disordered solid solutions containing substantial amounts of different elements randomly occupying sites in the crystal structure; ii) multicomponent intermetallic phases; iii) multi-phase compositions combining disordered solid solutions and intermetallic phases. These three classes of alloys have the potential to show a wide range of hydrogen storage behavior. While most of the works reported in the literature have focused on single-phase compositions [3,6–12,16–25], the presence of a multi-phase structure in multicomponent alloys might bring benefits for the hydrogenation behavior of these materials. For example, Chanchetti et al. [26] suggested that minor amounts of Laves C14 intermetallic phases in the  $Ti_{31}V_{26}Nb_{26}Zr_{12}M_5$  (M = Fe, Co, or Ni) alloys might have contributed to improving desorption behavior in these alloys in comparison to the  $Ti_{32.5}V_{27.5}Nb_{27.5}Zr_{12.5}$  alloy. The authors reported lower onset temperatures for hydrogen desorption in alloys containing minor amounts of Laves C14 phases. Also, Dangwal et al. [27] reported benefits of a dual-phase microstructure (BCC + C14) in predominant C14 multicomponent alloys, especially in the activation performance. The authors associated BCC + C14 interphase boundaries as possible sources of active sites for heterogenous hydride nucleation and, consequently, facilitate hydrogen absorption.

Considering Nb-rich multicomponent alloys, some BCC compositions have shown promising hydrogen storage performance. For example, Sakaki et al. [28] studied  $Nb_x(Ti_{0.7}Cr_{0.3})_{1-x}$  alloys (with x varying from 0.3 to 0.6) and found compositions that presented reversible hydrogen storage content of 1 H/M (ratio of hydrogen atoms to metal atoms) at 423 K. The authors reported that alloys with increased Nb content presented higher equilibrium pressures for hydrogen absorption and desorption. A similar trend was reported by Mayer Dias et al. [29] who also studied Ti-Nb-Cr compositions, fixing the Cr content in relation to the Nb/Ti ratio. It is worth noting that both studies combined hydride-forming elements (Nb and Ti) with a non-hydride-forming element (Cr) to obtain disordered BCC solid solutions with hydrogen absorption under moderate conditions of temperature and hydrogen pressure. It is also important to mention that Nb-rich BCC alloys are generally reported to absorb hydrogen via two absorption reactions, initially forming an intermediate BCC hydride or orthorhombic hydride that absorbs up to 1 H/M, and subsequently forming a face-centered cubic (FCC) hydride that absorbs up to 2 H/M [28,30,31]. Given the substantial difference in the thermodynamic stability of the BCC and FCC hydrides, it is commonly reported the reversibility of the FCC hydride and its related storage properties.

Motivated by these insights, in the present work we focused our investigations on the Nb-Cr-Mn system, exploring the addition of two non-hydride-forming elements to achieve Nb-rich alloys with room

temperature hydrogen storage reversibility. We employed a combination of the outlined strategies to reach our target. Using CALPHAD, we selected two compositions, namely  $Nb_{85}Cr_{10}Mn_5$  and  $Nb_{70}Cr_{20}Mn_{10}$ , aiming to obtain a single-phase BCC alloy and a multi-phase (BCC + Laves C14) alloy, both with high Cr and Mn contents in the BCC solid solution. This difference in the microstructural features of the alloys was designed to provide further analyses regarding the effect of BCC + Laves C14 interphases on the hydrogen storage properties of multicomponent alloys. Additionally, considering the highlighted correlations between VEC and the thermodynamic properties of BCC alloys [10,12], we adopted the VEC value of the  $Ti_{11}V_{30}Nb_{28}Cr_{31}$  alloy [8] as a reference for room temperature reversibility. Therefore, we selected compositions aiming for the formation of BCC solid solutions with a VEC of approximately 5.2.

## 2. Alloy design

The Nb-rich compositions displayed in Table 1 were selected via CALPHAD method using the Thermo-Calc® software and the TCHEA5 database. Fig. 1(a) and (b) show the evolution of the phase fractions as a function of temperature for the  $Nb_{85}Cr_{10}Mn_5$  and  $Nb_{70}Cr_{20}Mn_{10}$  compositions, respectively. Under equilibrium conditions, the  $Nb_{85}Cr_{10}Mn_5$  alloy was expected to solidify as a single-phase BCC structure, whereas the  $Nb_{70}Cr_{20}Mn_{10}$  alloy was predicted to solidify as a primary BCC phase followed by a eutectic-like constituent with a BCC + Laves C14 structure. Fig. 1(c) shows the isopleth  $Nb_{(100-3x)}Cr_{2x}Mn_x$ , which demonstrates the two solidification sequences predicted for the  $Nb_{85}Cr_{10}Mn_5$  and  $Nb_{70}Cr_{20}Mn_{10}$  alloys. Additionally, we carried out equilibrium calculations at 1550 °C (listed in Table 2) to estimate the chemical composition of the stable phases at the end of the solidification process. We assumed that the chemical compositional changes related to solid-state reactions would not be substantial below this temperature due to the rapid cooling rates provided by arc melting synthesis. According to the equilibrium calculations, both alloys would solidify as BCC solid solutions with a VEC of approximately 5.2. Moreover, the CALPHAD calculations predicted a 75 % BCC and 25 % Laves C14 structure in the  $Nb_{70}Cr_{20}Mn_{10}$  alloy.

## 3. Materials and methods

### 3.1. Synthesis

The  $Nb_{85}Cr_{10}Mn_5$  and  $Nb_{70}Cr_{20}Mn_{10}$  alloys were synthesized in an Edmund Bühlert GmbH arc melting furnace using high-purity elements (higher than 99.5 %) in an argon atmosphere. Ti-getter pieces were melted prior to each synthesis to minimize the oxygen content in the alloys. Twice the amount of Mn calculated for the nominal compositions was inserted into the furnace to compensate for Mn losses due to vaporization. After melting approximately 5 g of each composition, the ingots were re-melted four times to ensure chemical homogenization. Samples were removed for structural characterization and hydrogen absorption/desorption analyses. The remaining pieces were stored in an MBRAUN glovebox under an argon atmosphere with  $H_2O$  and  $O_2$  levels below 5 ppm.

### 3.2. Microstructural and structural characterization

Scanning Electron Microscopy (SEM) and Energy Dispersive X-ray

**Table 1**

Nominal compositions (at%) selected for this study and their respective VEC values.

Alloy	Nb (at%)	Cr (at%)	Mn (at%)	VEC
1	85	10	5	5.2
2	70	20	10	5.4

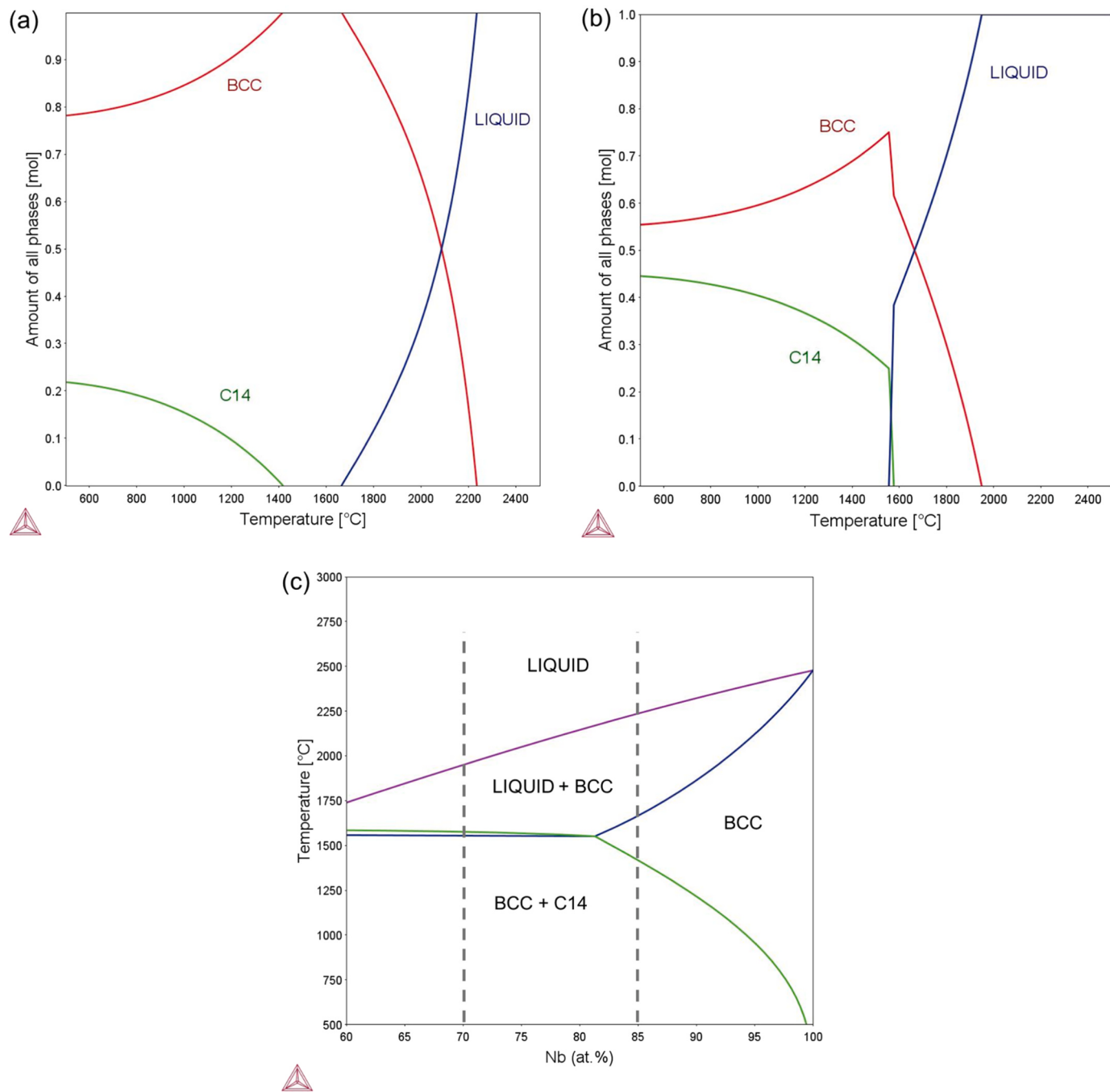


**Fig. 1.** CALPHAD calculations showing the evolution of phase fractions as a function of temperature for the (a) Nb<sub>85</sub>Cr<sub>10</sub>Mn<sub>5</sub> and (b) Nb<sub>70</sub>Cr<sub>20</sub>Mn<sub>10</sub> alloys and (c) isopleth phase diagram for the Nb<sub>(100-3x)</sub>Cr<sub>2x</sub>Mn<sub>x</sub> system.

**Table 2**

Calculated molar phase fractions and chemical compositions of the equilibrium phases of the Nb<sub>85</sub>Cr<sub>10</sub>Mn<sub>5</sub> and (b) Nb<sub>70</sub>Cr<sub>20</sub>Mn<sub>10</sub> alloys at 1550 °C (Thermo-Calc software® and TCHEA5 database).

Alloy	BCC					Laves C14			
	Phase fraction	Nb (at%)	Cr (at%)	Mn (at%)	VEC	Phase fraction	Nb (at%)	Cr (at%)	Mn (at%)
Nb <sub>85</sub> Cr <sub>10</sub> Mn <sub>5</sub>	1.00	85.0	10.0	5.0	5.20	-	-	-	-
Nb <sub>70</sub> Cr <sub>20</sub> Mn <sub>10</sub>	0.75	81.3	12.7	6.0	5.25	0.25	36.5	41.5	22.0

Spectroscopy (EDS) analyses were performed on the as-cast ingots using a Philips XL-30 FEG scanning electron microscope coupled with a Bruker Nano XFlash 6|60 EDX detector. The microstructure of the alloys was analyzed by acquiring Backscattered Electron (BSE) images and

measuring the chemical compositional homogeneity in different regions of the samples. The X-ray Diffraction (XRD) technique was used to identify the phases present in the as-cast condition and after hydrogen absorption/desorption reactions. XRD patterns were acquired in a

Bruker D8 Advance Eco diffractometer with Cu-K $\alpha$  radiation ( $K_{\alpha 1}=1.5406 \text{ \AA}$ ,  $K_{\alpha 2}=1.5444 \text{ \AA}$ ). Rietveld refinements were performed using the General Structure Analysis System II [32] (GSAS II) software to provide information about the phase fractions in the analyzed samples and to estimate their lattice parameters. The refined parameters were background, lattice parameter, crystallite size, and isotropic microstrain.

### 3.3. Hydrogen absorption/desorption analyses

Volumetric measurements of hydrogen absorption and desorption were performed using a Sieverts-type apparatus (SETARAM® PCT-Pro). For each experiment, samples of the ingots were crushed into small pieces using a mortar and pestle and loaded into a dedicated sample holder. Kinetics measurements were performed at room temperature by subjecting the samples to approximately 25 bar of hydrogen. Pressure-Composition-Temperature (PCT) diagrams were obtained for each alloy by measuring Pressure-Composition-Isotherms at 30, 50, and 70 °C under absorption and desorption conditions between equilibrium pressures of 0.01 and 75 bar. A low-pressure transducer (with a detection limit between 0.001 and 0.01 bar) was applied to measure the equilibrium pressures lower than 5 bar, whereas a high-pressure transducer was utilized to measure the equilibrium pressures higher than 5 bar. This procedure provided precise measurements of the absorbed/desorbed capacities for the entire range of pressures analyzed. Van't Hoff analyses were carried out using Eq. (2) to calculate the enthalpy and entropy related to the BCC hydride  $\leftrightarrow$  FCC hydride reaction:

$$\frac{1}{2} \ln \left( \frac{P_{eq}}{P^o} \right) = \frac{\Delta H}{RT} - \frac{\Delta S}{R} \quad (2)$$

where  $P_{eq}$  is the equilibrium pressure of each PCI plateau,  $P^o$  is the standard pressure value to define the reference state ( $P^o = 1 \text{ atm}$ ),  $R$  is the universal gas constant,  $\Delta H$  and  $\Delta S$  are the enthalpy and entropy per mol of H related to the hydride formation and decomposition reactions. Moreover, room temperature hydrogen storage reversibility was investigated via cycling experiments. The absorption cycles were conducted subjecting the samples to approximately 35 bar of hydrogen, whereas the desorption cycles were carried out under dynamic vacuum for 20 minutes at room temperature.

## 4. Results and discussion

### 4.1. Structural characterization

XRD patterns of the as-cast alloys are presented in Fig. 2. The patterns indicate that the Nb<sub>85</sub>Cr<sub>10</sub>Mn<sub>5</sub> alloy formed a BCC structure, whereas the Nb<sub>70</sub>Cr<sub>20</sub>Mn<sub>10</sub> alloy formed a multi-phase (BCC + Laves C14) structure, as predicted by the CALPHAD calculations. The Rietveld refinements data related to these patterns are shown in Fig. S1 and Table S1 of the supplementary data file. Lattice parameters and phase fractions obtained via Rietveld refinements are listed in Table 3. It is worth noting that the estimated concentration of Laves C14 in the Nb<sub>70</sub>Cr<sub>20</sub>Mn<sub>10</sub> alloy (22 wt%) is quite consistent with CALPHAD predictions (25%). Moreover, a small difference in the BCC lattice parameters was observed between the Nb<sub>85</sub>Cr<sub>10</sub>Mn<sub>5</sub> and Nb<sub>70</sub>Cr<sub>20</sub>Mn<sub>10</sub> alloy (3.285 Å and 3.256 Å respectively). We assumed that this BCC lattice variation was related to the different concentrations of Cr and Mn in solid solution, as predicted by CALPHAD, since increased contents of Mn (atomic radius of 1.27–1.35 Å [4,33]) and Cr (atomic radius of 1.25–1.28 Å [4,33]) in solid solution reduces the lattice parameters of the BCC phase, given the larger atomic radius of Nb (1.43–1.46 Å [4,33]).

SEM analyses displayed in Fig. 3(a) and (b) illustrate the dendritic morphology observed in both as-cast alloys. The dendritic morphology is frequently reported for multicomponent alloys and Nb-rich alloys

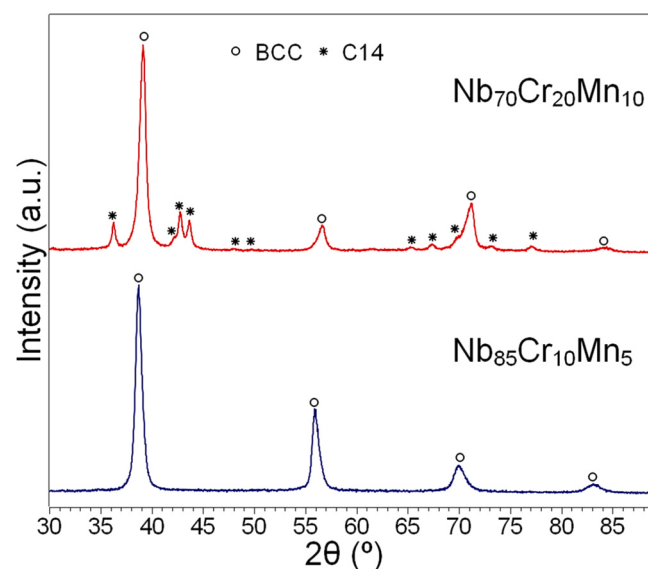


Fig. 2. XRD patterns of the as-cast Nb<sub>85</sub>Cr<sub>10</sub>Mn<sub>5</sub> and Nb<sub>70</sub>Cr<sub>20</sub>Mn<sub>10</sub> alloys.

synthesized via electric arc melting due to the rapid solidification process [3,7,8,10,12,17,18,25]. EDS mapping shows that Cr and Mn partitioning occurred in both alloys, leading to interdendritic regions rich in those elements. Fig. 3(c) and (d) show microstructural features indicating the eutectic formation in both alloys. It is worth noting the refined morphology of the eutectic structure.

Although thermodynamic calculations indicated that the Nb<sub>85</sub>Cr<sub>10</sub>Mn<sub>5</sub> alloy would crystallize as a single-phase BCC under equilibrium conditions, they also predicted a large solidification interval (approximately 600 °C). Therefore, considerable solute partitioning probably occurred under non-equilibrium conditions, resulting in the formation of the observed minor fraction of eutectic mixture. Furthermore, we assume that the Laves C14 phase in the eutectic constituent of the Nb<sub>85</sub>Cr<sub>10</sub>Mn<sub>5</sub> alloy could not be detected via XRD due to the low concentration of this phase. Silva et al. [12] and Strozi et al. [7] also reported similar issues in the design via CALPHAD of the (TiVNb)<sub>96.2</sub>Ni<sub>3.8</sub> and the (TiVNb)<sub>60</sub>Cr<sub>40</sub> alloys due to non-equilibrium solidification conditions. In the case of the (TiVNb)<sub>96.2</sub>Ni<sub>3.8</sub> alloy, a minor fraction of the TiNi-rich B2 phase was formed during solidification, although equilibrium calculations suggested the formation of a single-phase BCC structure. For the (TiVNb)<sub>60</sub>Cr<sub>40</sub> alloy, a substantial amount of a secondary Laves C15 phase formed was associated with increased levels of Cr partitioned during solidification, which prevented the obtention of a predominant BCC structure.

Quantitative EDS measurements, summarized in Table 4, provide information regarding the overall chemical composition of the alloys and their dendritic/eutectic regions. These analyses revealed small deviations of the overall alloys' compositions compared to the nominal compositions. These small deviations were expected given the synthesis methodology and the uncertainty of Mn losses due to vaporization. Considering the solidification sequences predicted via CALPHAD and the microstructure features observed via SEM, we assumed the bright and dark regions of the alloys' microstructure corresponded to the BCC and Laves C14 phases, respectively. Therefore, we observe that the BCC and Laves C14 concentrations in the microstructure of the Nb<sub>70</sub>Cr<sub>20</sub>Mn<sub>10</sub> alloy are quite consistent with the equilibrium calculations via CALPHAD and the values obtained via Rietveld refinements. Likewise, the composition of the dendritic regions from the Nb<sub>70</sub>Cr<sub>20</sub>Mn<sub>10</sub> alloy was nearly identical to the BCC composition listed in Table 2. On the other hand, since the solidification process of the Nb<sub>85</sub>Cr<sub>10</sub>Mn<sub>5</sub> alloy seemed to follow non-equilibrium conditions, the fractions of BCC and Laves C14 phases and the chemical composition of the BCC phase presented

**Table 3**

Phase fractions and lattice parameters determined by Rietveld refinement analyses of the as-cast, hydrogenated, and cycled Nb<sub>85</sub>Cr<sub>10</sub>Mn<sub>5</sub> and Nb<sub>70</sub>Cr<sub>20</sub>Mn<sub>10</sub> alloys.

Sample	BCC (wt%)	FCC (wt%)	C14 (wt%)	$a_{\text{BCC}}$ (Å)	$a_{\text{FCC}}$ (Å)	$a_{\text{C14}}$ (Å)	$c_{\text{C14}}$ (Å)
Nb <sub>85</sub> Cr <sub>10</sub> Mn <sub>5</sub> as-cast	100	—	—	3.285(1)	—	—	—
Nb <sub>70</sub> Cr <sub>20</sub> Mn <sub>10</sub> as-cast	78	—	22	3.256(1)	—	4.950(1)	8.122(1)
Nb <sub>85</sub> Cr <sub>10</sub> Mn <sub>5</sub> 1st hydrogenation	10	90	—	3.419(1)	4.546(1)	—	—
Nb <sub>70</sub> Cr <sub>20</sub> Mn <sub>10</sub> 1st hydrogenation	24	51	25	3.381(1)	4.523(1)	4.946(1)	8.114(1)
Nb <sub>85</sub> Cr <sub>10</sub> Mn <sub>5</sub> 20th hydrogenation	27	73	—	3.411(1)	4.543(1)	—	—
Nb <sub>70</sub> Cr <sub>20</sub> Mn <sub>10</sub> 20th hydrogenation	20	52	28	3.386(1)	4.528(1)	4.948(1)	8.116(1)

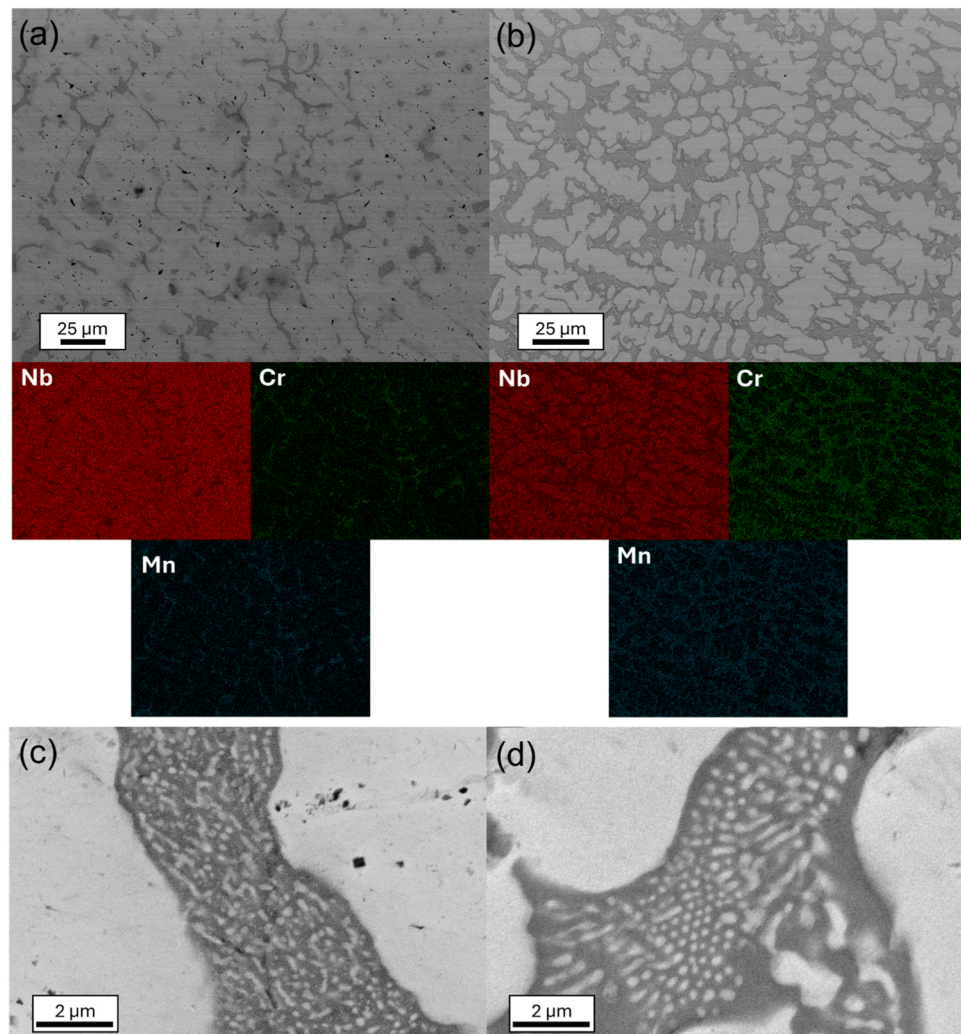


**Fig. 3.** Overall microstructure and EDS mapping of the as-cast (a) Nb<sub>85</sub>Cr<sub>10</sub>Mn<sub>5</sub> and (b) Nb<sub>70</sub>Cr<sub>20</sub>Mn<sub>10</sub> alloys; Eutectic microstructural features found in the (c) Nb<sub>85</sub>Cr<sub>10</sub>Mn<sub>5</sub> and (d) Nb<sub>70</sub>Cr<sub>20</sub>Mn<sub>10</sub> alloys.

slight deviations in comparison to the CALPHAD predictions.

Despite these minor differences, it is important to highlight that we successfully achieved the main objective regarding the chemical compositional targets of the BCC phases. BCC compositions with VEC  $\sim$  5.2 were obtained in both alloys. The EDS measurements displayed in Table 4 confirmed that the dendritic regions of both alloys presented compositions with VEC varying between 5.15 and 5.23. Moreover, it is worth mentioning that the Nb<sub>70</sub>Cr<sub>20</sub>Mn<sub>10</sub> alloy indeed presented a BCC composition slightly more concentrated in Cr and Mn than the

Nb<sub>85</sub>Cr<sub>10</sub>Mn<sub>5</sub> alloy, supporting the assumption on the effect of chemical compositional differences on lattice parameters observed via XRD analyses.

#### 4.2. Hydrogen sorption analyses

Fig. 4(a) exhibits the hydrogen absorption kinetics curves obtained at room temperature for both alloys. The measurements demonstrate that the alloys were easily hydrogenated without the need for an

**Table 4**

EDS analyses of the overall, dendritic, and eutectic regions of the as-cast Nb<sub>85</sub>Cr<sub>10</sub>Mn<sub>5</sub> and Nb<sub>70</sub>Cr<sub>20</sub>Mn<sub>10</sub> alloys.

Region analyzed	Nb <sub>85</sub> Cr <sub>10</sub> Mn <sub>5</sub>				Nb <sub>70</sub> Cr <sub>20</sub> Mn <sub>10</sub>			
	Nb (at %)	Cr (at %)	Mn (at%)	VEC	Nb (at %)	Cr (at %)	Mn (at%)	VEC
	(%)	(%)			(%)	(%)		
Overall	81.3	11.5	7.2	5.26	66.9	22.0	11.2	5.45
	81.6	10.9	7.5	5.26	66.2	22.6	11.2	5.45
	83.3	10.4	6.3	5.23	67.3	21.9	10.8	5.44
Dendritic	89.0	7.1	3.9	5.15	83.9	11.2	4.9	5.21
	87.3	8.3	4.5	5.18	82.2	12.4	5.3	5.22
	88.9	7.2	3.9	5.15	82.0	12.6	5.4	5.23
Eutectic	49.3	27.9	22.7	5.73	50.3	33.0	16.7	5.66
	46.4	28.7	24.8	5.78	49.3	34.2	16.5	5.67
	47.2	28.6	24.2	5.77	49.2	33.3	17.6	5.69

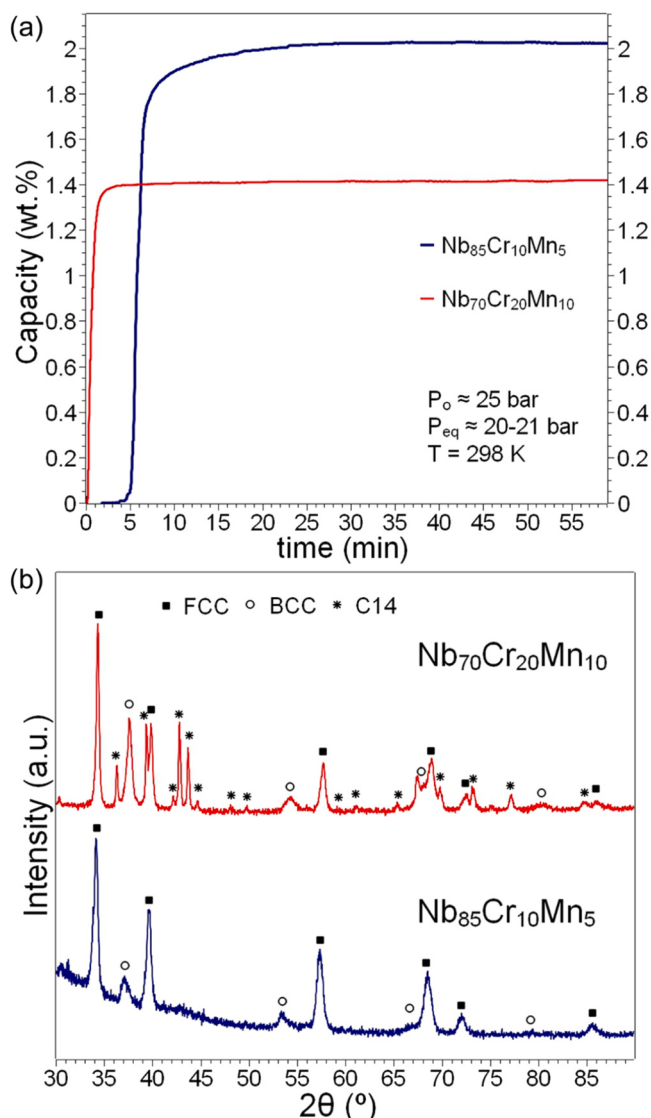


Fig. 4. (a) Hydrogen absorption kinetics measurements of the Nb<sub>85</sub>Cr<sub>10</sub>Mn<sub>5</sub> and Nb<sub>70</sub>Cr<sub>20</sub>Mn<sub>10</sub> alloys (b) XRD patterns of the hydrogenated Nb<sub>85</sub>Cr<sub>10</sub>Mn<sub>5</sub> and Nb<sub>70</sub>Cr<sub>20</sub>Mn<sub>10</sub> alloys.

activation treatment, reaching hydrogen storage capacities between 1.4 and 2.1 wt% of H ( $P_{eq} \sim 20\text{--}21$  bar), which correspond to 1.1 and 1.8 H/ $M$ , respectively. Interestingly, the Nb<sub>70</sub>Cr<sub>20</sub>Mn<sub>10</sub> alloy presented faster hydrogen absorption behavior, with a shorter incubation time, than the

Nb<sub>85</sub>Cr<sub>10</sub>Mn<sub>5</sub> alloy. This faster absorption reaction could be correlated to the fraction of the eutectic constituent, which provides a high concentration of interfaces between the BCC and Laves C14 phases. These interfaces might benefit the processes involved in heterogenous hydride nucleation and growth. According to Dangwal et al. [27], interphase boundaries had a significant effect on the hydrogen storage activation of the TiV<sub>1.5</sub>ZrCr<sub>0.5</sub>MnFeNi (C14 + 4 vol% BCC phases) in comparison to the TiV<sub>1.5</sub>Zr<sub>1.5</sub>CrMnFeNi (single C14 phase). The authors reported that the single-phase alloy needed to be activated at 673 K to absorb hydrogen, whereas the multi-phase alloy could absorb hydrogen at room temperature without an activation process. We believe that BCC + C14 interfaces might also play a significant role in the hydrogen storage behavior of multicomponent alloy with predominant BCC microstructure. However, hydrogen storage activation and kinetics of metals/alloys have been correlated to several factors such as surface oxidation, particle size, and other microstructural features [34–41].

XRD analyses of the hydrogenated samples indicated the formation of the intermediate hydride (identified as BCC) and the dihydride (identified as FCC) in both samples, as presented in Fig. 4(b). We acknowledge that intermediate hydrides in Nb-rich solid solutions might also be identified with an orthorhombic structure (slightly distorted BCC) but, in the present work, the BCC structure was considered because it provided better XRD fittings from Rietveld refinement analyses.

The Rietveld refinements data related to the XRD patterns of the hydrogenated samples are exhibited in Fig. S2 and Table S1 of the supplementary file. The summarized results of lattice parameters and phase concentrations are listed in Table 3. The increased lattice parameters of the BCC phases in the hydrogenated samples in comparison to the as-cast samples confirm the formation of the intermediate hydrides. The presence of these intermediate hydrides in both samples indicates that the FCC hydrides were partially destabilized after removing the samples from the high-pressure environment. The Nb<sub>70</sub>Cr<sub>20</sub>Mn<sub>10</sub> alloy showed a higher concentration of BCC hydride (~24 wt%), indicating higher equilibrium plateau pressures in comparison to the Nb<sub>85</sub>Cr<sub>10</sub>Mn<sub>5</sub> alloy.

The lattice parameters estimated for the Laves C14 phases in the hydrogenated sample were virtually the same as those in the as-cast sample. This provides evidence that the Laves C14 phase has not experienced any significant hydrogen absorption. This conclusion is also supported by the maximum hydrogen storage capacities observed via kinetics measurements, as the difference in the maximum storage capacity of the alloys is roughly proportional to the difference in Laves C14 concentration (approximately 25%).

PCT diagrams of the Nb<sub>85</sub>Cr<sub>10</sub>Mn<sub>5</sub> and Nb<sub>70</sub>Cr<sub>20</sub>Mn<sub>10</sub> alloys are displayed in Fig. 5(a) and (b), respectively. Similar two-step reactions were observed: initially, the alloys absorb hydrogen under very low equilibrium pressures (lower than the detection limit provided by the transducers), and later, at higher equilibrium pressures, a plateau is formed, reaching the maximum hydrogen storage capacity of the alloys. As discussed in the introduction section, this behavior agrees with the reported hydrogenation process of other BCC alloys following the BCC and FCC hydride formation. Therefore, these measurements also support the assumption that the Laves C14 phases have not absorbed/desorbed any significant amount of hydrogen.

It is also worth mentioning that the maximum storage capacities observed in the PCI curves are reduced with increasing the PCI temperature. This is a well-known effect related to thermodynamic aspects of metal-hydrogen systems. The thermodynamic equilibrium of these systems is dependent on the chemical potential of hydrogen and metal elements on the different phases co-existing in the system. These chemical potentials are affected by the temperature conditions, which consequently change the composition of hydrogen in equilibrium in the stable phases. The readers are encouraged to refer to [15,42] for a detailed explanation.

Moreover, a hysteresis effect was observed in the PCI curves for both alloys, causing differences of approximately one order of magnitude in

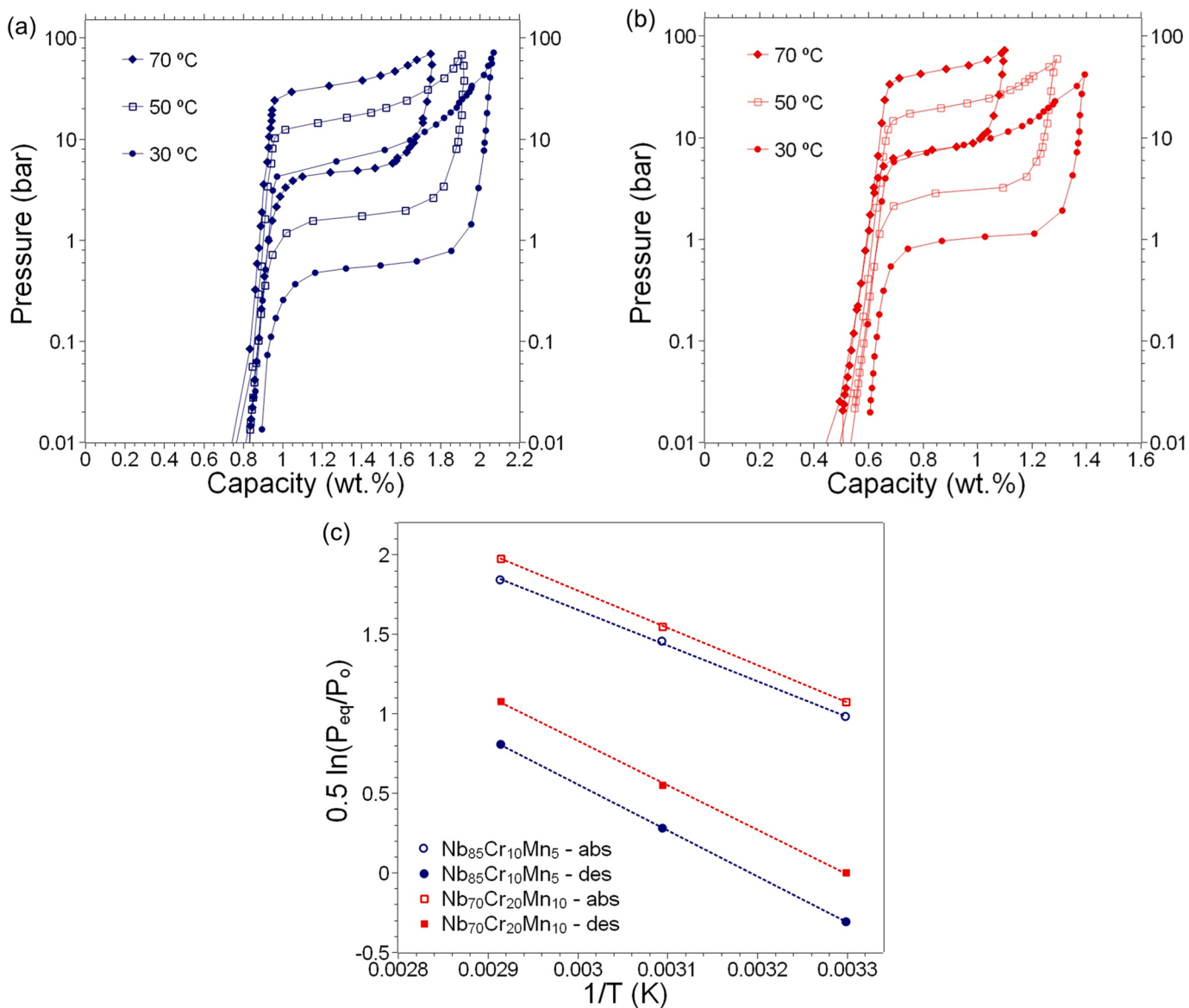


**Fig. 5.** Pressure-Composition-Temperature diagrams of the (a) Nb<sub>85</sub>Cr<sub>10</sub>Mn<sub>5</sub> alloy and (b) Nb<sub>70</sub>Cr<sub>20</sub>Mn<sub>10</sub> alloy and their corresponding (c) Van't Hoff plots.

the equilibrium pressures for absorption and desorption. This effect has been reported in other BCC alloys and is generally associated with factors such as plastic deformation, defect generation, particle size, and elastic strain energy [7,8,12,43]. Table 5 provides the values of equilibrium pressures selected for the Van't Hoff calculations, considering the middle of the plateau at 1.45 wt% for the Nb<sub>85</sub>Cr<sub>10</sub>Mn<sub>5</sub> alloy and 0.98 wt% for the Nb<sub>70</sub>Cr<sub>20</sub>Mn<sub>10</sub> alloy. Both alloys presented high equilibrium pressures for hydrogen absorption/desorption considering the BCC hydride  $\leftrightarrow$  FCC hydride reactions. The Nb<sub>70</sub>Cr<sub>20</sub>Mn<sub>10</sub> alloy presented slightly higher equilibrium pressures than the Nb<sub>85</sub>Cr<sub>10</sub>Mn<sub>5</sub> alloy, which can be correlated to the differences in Cr and Mn concentration in the BCC phases and, consequently, the VEC.

Remarkably, the PCI at 30 °C from the Nb<sub>70</sub>Cr<sub>20</sub>Mn<sub>10</sub> alloy exhibited equilibrium desorption pressures at approximately 1 bar, indicating the possibility of room temperature hydrogen storage reversibility at moderate hydrogen pressure conditions. Table 5 also comprises the thermodynamic properties (enthalpies and entropies values for the formation and decomposition of the FCC hydride) obtained via Van't Hoff analyses and Van't Hoff plot (Fig. 5(c)). The thermodynamic values observed for the Nb<sub>85</sub>Cr<sub>10</sub>Mn<sub>5</sub> and Nb<sub>70</sub>Cr<sub>20</sub>Mn<sub>10</sub> alloys are very similar to the values reported for the Ti<sub>11</sub>V<sub>30</sub>Nb<sub>28</sub>Cr<sub>31</sub> [8] alloy (-18/22 kJ/mol H and -71/75 J/K.mol H), which was the main target for this work.

Therefore, our strategy proved to be efficient in achieving room temperature hydrogen storage reversibility. Moreover, it is worth

**Table 5**

Equilibrium absorption/desorption pressures selected for Van't Hoff analyses and thermodynamic properties (enthalpies and entropies values for the formation and decomposition of the FCC hydride) calculated via Eq. (2).

Alloy	Absorption P <sub>eq</sub> (bar)			Desorption P <sub>eq</sub> (bar)			$\Delta H_{BCC \leftrightarrow FCC}$ (kJ/mol H)		$\Delta S_{BCC \leftrightarrow FCC}$ (J/K.mol H)	
	30 °C	50 °C	70 °C	30 °C	50 °C	70 °C	Abs	Des	Abs	Des
Nb <sub>85</sub> Cr <sub>10</sub> Mn <sub>5</sub>	7.05	18.20	39.40	0.54	1.75	5.00	-19	24	-70	77
Nb <sub>70</sub> Cr <sub>20</sub> Mn <sub>10</sub>	8.59	22.10	52.00	1.00	3.00	8.60	-19	23	-73	77

mentioning that the results obtained in the present work reinforce the hypothesis/correlation suggested by Silva et al. [12] supporting that the VEC parameter is somehow correlated to the thermodynamic hydrogenation behavior of multicomponent BCC alloys. Table 6 summarizes and compares the results obtained in this work with other Nb-rich multicomponent alloys exhibiting the correlation of VEC values of the BCC compositions with the enthalpy values for the formation and decomposition of the corresponding FCC hydrides. It is indicated that in Nb-rich BCC compositions, the increase in the VEC values consistently decreases the formation and decomposition enthalpies of the FCC hydride (reaching approximately  $-20 \text{ kJ/mol H}$  and  $23 \text{ kJ/mol H}$  respectively, for our compositions) suggesting hydrogen storage reversibility at room temperature.

Fig. 6 shows the cycling measurements of the  $\text{Nb}_{85}\text{Cr}_{10}\text{Mn}_5$  and  $\text{Nb}_{70}\text{Cr}_{20}\text{Mn}_{10}$  alloys performed at room temperature. The results indicate that the kinetic behavior of both alloys improves after the first cycle, reaching the maximum storage capacity in shorter periods of time. After the first cycle, the  $\text{Nb}_{85}\text{Cr}_{10}\text{Mn}_5$  shows a stable reversible capacity of 1.2 wt% of H ( $P_{\text{eq}} \sim 29 \text{ bar}$ ) of H, which corresponds to roughly the same capacity observed for the BCC hydride  $\leftrightarrow$  FCC hydride reaction in the PCI measurement at  $30^\circ\text{C}$ . Similarly, the  $\text{Nb}_{70}\text{Cr}_{20}\text{Mn}_{10}$  alloy reached a storage capacity of 0.9 wt% of H ( $P_{\text{eq}} \sim 30 \text{ bar}$ ) in the second cycle of absorption, which also corresponds to the capacity observed for the BCC hydride  $\leftrightarrow$  FCC hydride plateau in the PCI measurement at  $30^\circ\text{C}$ . However, a small reduction in the storage capacity was observed for this alloy over the cycles, reducing the maximum storage capacity to 0.8 wt% of H ( $P_{\text{eq}} \sim 31 \text{ bar}$ ) after 20 cycles.

To assess possible structural changes over hydrogen absorption/desorption cycling, we characterized the samples of the  $\text{Nb}_{85}\text{Cr}_{10}\text{Mn}_5$  and  $\text{Nb}_{70}\text{Cr}_{20}\text{Mn}_{10}$  alloy via XRD analyses after cycling. Fig. 7 displays the XRD patterns of the hydrogenated samples after cycling. Rietveld refinements data are shown in Fig. S3 and Table S1 of the supplementary material file, and the estimated phase fraction and lattice parameters are listed in Table 3. A higher concentration of the BCC hydride was identified in the hydrogenated samples of the  $\text{Nb}_{85}\text{Cr}_{10}\text{Mn}_5$  alloy after cycling compared to the sample after the first hydrogenation. Since the storage capacity of this alloy has not changed over cycling, we assume that a higher amount of FCC hydride was destabilized after removing this sample from the high-pressure environment. This might indicate changes in the hysteresis magnitude over cycling, resulting in higher equilibrium desorption pressures.

On the other hand, the XRD pattern of the  $\text{Nb}_{70}\text{Cr}_{20}\text{Mn}_{10}$  alloy has not presented a substantial difference in the amount of FCC hydride after cycling. Only minor differences in the phase fractions of the BCC and Laves C14 phases were observed comparing the XRD patterns before and after cycling. Based on these results, the sources for the slight reduction in hydrogen storage capacity of the  $\text{Nb}_{70}\text{Cr}_{20}\text{Mn}_{10}$  alloy are not clear.

**Table 6**  
Comparison of enthalpy values for the FCC hydride formation/decomposition in Nb-rich alloys with their VEC values.

Alloy	Nominal VEC	VEC of the BCC phase	$\Delta H_{\text{BCC} \rightarrow \text{FCC}}$ (kJ/mol H)	$\Delta H_{\text{FCC} \rightarrow \text{BCC}}$ (kJ/mol H)
$\text{Ti}_{20}\text{Zr}_{20}\text{Hf}_{20}\text{Nb}_{40}$ [44]	4.40	—	-38	—
$\text{Ti}_{28.3}\text{V}_{1.3}\text{Nb}_{55.4}\text{Cr}_{15}$ [15]	4.87	4.85	-32	34
$\text{Ti}_{25}\text{Nb}_{43.8}\text{Cr}_{31.3}$ [29]	5.07	5.00	-24	31
$\text{Ti}_{17.7}\text{Nb}_{52.9}\text{Cr}_{29.4}$ [29]	5.12	5.06	-24	33
$\text{Ti}_{11.1}\text{Nb}_{61.1}\text{Cr}_{27.8}$ [29]	5.17	5.07	-23	27
$\text{Nb}_{85}\text{Cr}_{10}\text{Mn}_5$ *present work	5.2	5.16	-19	24
$\text{Nb}_{70}\text{Cr}_{20}\text{Mn}_{10}$ *present work	5.25	5.22	-19	23

However, the deterioration of hydrogen storage capacity in metals and alloys over cycling has been attributed to several factors such as disproportionation, crystallite size refinement, higher defect concentration, and increase of lattice strain [24,45–48]. For instance, Strozi et al. [48] has recently investigated the cycling performance of the  $\text{TiVNbCr}$  BCC multicomponent alloy, using positron annihilation spectroscopy and pair distribution function analyses. The authors suggested that the fade in capacity could be associated with the formation of vacancy clusters and dislocations over cycling.

Considering the main results obtained in this work, it is important to discuss and emphasize a few points. 1) Using a simple strategy combining CALPHAD method and the correlation of the BCC phase VEC parameter with thermodynamic hydrogen storage properties, we were able to achieve room temperature hydrogen storage reversibility in Nb-rich alloys under moderate conditions of hydrogen pressure. This strategy can be easily applied to other multicomponent BCC + C14 systems. 2) CALPHAD is a valuable thermodynamic computational tool for designing alloys for hydrogen storage applications. The strategy reported in this work shows a clear example of how to combine this computational method with literature knowledge to achieve specific hydrogen storage performance in novel materials. 3) The limited gravimetric storage capacity (1.4–2.1 wt% of H) of the Nb-rich alloys investigated in this work is associated with two main factors: i) The high molar weight of these alloys, given the Nb molar weight ( $\sim 92.9 \text{ g/mol}$ ); ii) The amount of Laves C14 phase, that reduced the maximum storage capacity especially for the  $\text{Nb}_{70}\text{Cr}_{20}\text{Mn}_{10}$  alloy. 4) Finding other multicomponent systems that contain similar solidification characteristics might be helpful in designing alloys rich in other elements for various hydrogen storage applications. The presence of BCC + C14 interfaces seems to play a significant role in hydrogen storage activation and kinetics of absorption. In this context, the refined morphology of eutectic microconstituents containing BCC + C14 phases can potentially improve the hydrogen storage properties of other similar alloy systems. 5) Although, in the present work, the Laves C14 intermetallic phase has not presented any significant level of hydrogen absorption, multicomponent systems combining BCC + Laves C14 have great potential to improve hydrogen storage properties (kinetics and thermodynamic properties) and, therefore, expand the number of candidate compositions for hydrogen storage applications. However, obtaining compatible equilibrium pressures in the BCC and Laves C14 phases for specific hydrogen storage applications might be a relevant challenge.

## 5. Conclusions

The main conclusions obtained from this work are listed as follows:

- Combining the CALPHAD method with a strategy based on selecting alloy compositions that form BCC solid solutions with a VEC of approximately 5.2 has proven to be a remarkably effective approach for obtaining Nb-rich alloys with room temperature hydrogen storage reversibility.
- We have successfully synthesized Nb-rich alloys of the Nb-Cr-Mn system with a predominant BCC structure and with minor amounts of a eutectic microconstituent composed of BCC + Laves C14 phases.
- The alloys, namely  $\text{Nb}_{85}\text{Cr}_{10}\text{Mn}_5$  and  $\text{Nb}_{70}\text{Cr}_{20}\text{Mn}_{10}$ , were easily hydrogenated at room temperature without the need for an activation treatment and exhibited moderate absorption/desorption equilibrium pressures at room temperature.
- Upon hydrogenation, the  $\text{Nb}_{85}\text{Cr}_{10}\text{Mn}_5$  and  $\text{Nb}_{70}\text{Cr}_{20}\text{Mn}_{10}$  alloys readily reached maximum storage capacities of 2.1 and 1.4 wt% of H ( $\sim 1.1\text{--}1.8 \text{ H/M}$ ), respectively, forming FCC hydrides. Faster hydrogen absorption behavior was observed for the  $\text{Nb}_{70}\text{Cr}_{20}\text{Mn}_{10}$  alloy, indicating that BCC + C14 interfaces might bring benefits to the kinetic behavior of these alloys.
- Cycling measurements at room temperature showed that the  $\text{Nb}_{85}\text{Cr}_{10}\text{Mn}_5$  alloy reached a stable reversible capacity of 1.2 wt% of H after 20 cycles.

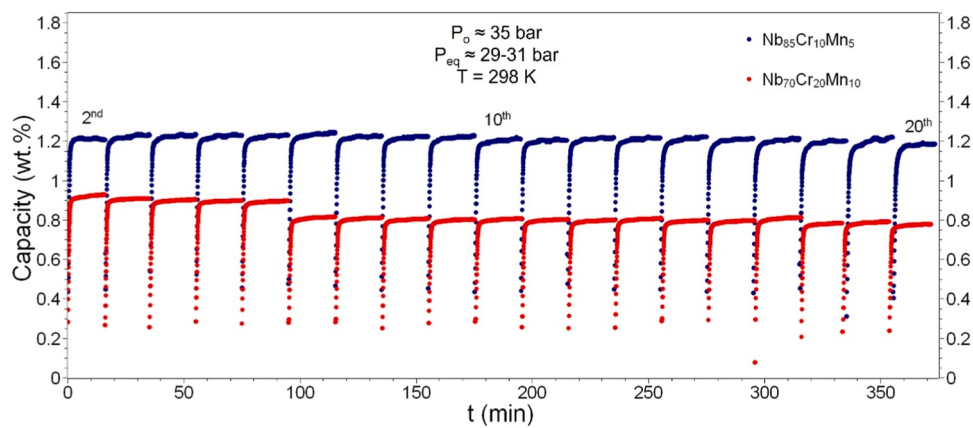


**Fig. 6.** Room temperature hydrogen absorption/desorption cycling of the Nb<sub>85</sub>Cr<sub>10</sub>Mn<sub>5</sub> and Nb<sub>70</sub>Cr<sub>20</sub>Mn<sub>10</sub> alloys (each desorption cycle was carried out under dynamic vacuum for 20 minutes).

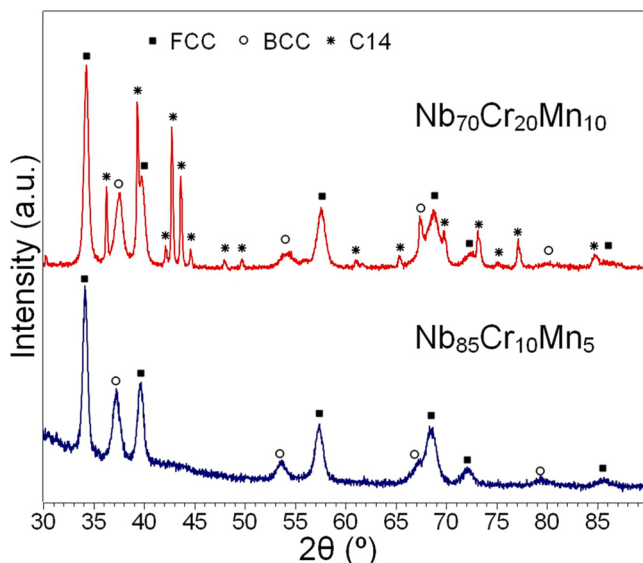


**Fig. 7.** XRD patterns of the Nb<sub>85</sub>Cr<sub>10</sub>Mn<sub>5</sub> and Nb<sub>70</sub>Cr<sub>20</sub>Mn<sub>10</sub> alloys after cycling.

H ( $\sim 1$  H/M) after 20 cycles, whereas the Nb<sub>70</sub>Cr<sub>20</sub>Mn<sub>10</sub> alloy exhibited a slight reduction in capacity, reaching 0.8 wt% of H ( $\sim 0.6$  H/M) after 20 cycles.

#### CRediT authorship contribution statement

**Guilherme Zepon:** Writing – review & editing, Validation, Supervision, Methodology, Funding acquisition, Formal analysis, Conceptualization. **Walter José Botta:** Writing – review & editing, Validation, Supervision, Methodology, Funding acquisition, Formal analysis, Conceptualization. **Bruno Hessel Silva:** Writing – review & editing, Writing – original draft, Validation, Methodology, Investigation, Formal analysis, Conceptualization.

#### Declaration of Competing Interest

The authors declare that they have no known competing financial interests or personal relationships that could have appeared to influence the work reported in this paper.

#### Data availability

Data will be made available on request.

#### Acknowledgments

This work was financed in part by the Serrapilheira Institute (grant number Serra-1709-17362), in part by the Brazilian National Council for Scientific and Technological Development – CNPq (Project number: 407906/2022-3 Process number: 350914/2023-0), and in part by the Studies and Project Funding, FINEP (grant number: FINEP 01.22.0177.00). This study was also financed in part by the Coordenação de Aperfeiçoamento de Pessoal de Nível Superior - Brasil (CAPES) - Finance Code 001, Federal University of São Carlos, Graduate Program in Materials Science and Engineering. The authors are grateful to the Laboratory of Structural Characterization (LCE/DEMa/UFSCar) for the electron microscopy and X-ray diffraction facilities.

#### Appendix A. Supporting information

Supplementary data associated with this article can be found in the online version at doi:10.1016/j.jallcom.2024.176187.

#### References

- [1] C. Drawer, J. Lange, M. Kaltschmitt, Metal hydrides for hydrogen storage – identification and evaluation of stationary and transportation applications, *J. Energy Storage* 77 (2024), <https://doi.org/10.1016/j.est.2023.109988>.
- [2] J. Bellosta von Colbe, J.R. Ares, J. Barale, M. Baricco, C. Buckley, G. Capurso, et al., Application of hydrides in hydrogen storage and compression: achievements, outlook and perspectives, *Int. J. Hydrogen Energy* 44 (2019) 7780–7808, <https://doi.org/10.1016/j.ijhydene.2019.01.104>.
- [3] M. Felderhoff, F. Marques, M. Balcerzak, F. Winkelmann, G. Zepon, Review and outlook on high-entropy alloys for hydrogen storage, *Energy Environ. Sci.* (2021), <https://doi.org/10.1039/DLEE01543e>.
- [4] D.B. Miracle, O.N. Senkov, A critical review of high entropy alloys and related concepts, *Acta Mater.* 122 (2017) 448–511, <https://doi.org/10.1016/j.actamat.2016.08.081>.
- [5] T.R. Somo, M.V. Lototskyy, V.A. Yartys, M.W. Davids, S.N. Nyamsi, Hydrogen storage behaviours of high entropy alloys: a review, *J. Energy Storage* 73 (2023), <https://doi.org/10.1016/j.est.2023.108969>.
- [6] R.B. Strozi, D.R. Leiva, G. Zepon, W.J. Botta, J. Huot, Effects of the chromium content in (Tivnb)100-xcrx body-centered cubic high entropy alloys designed for hydrogen storage applications, *Energies* 14 (2021), <https://doi.org/10.3390/en14113068>.
- [7] R.B. Strozi, B.H. Silva, D.R. Leiva, C. Zlatea, W.J. Botta, G. Zepon, Tuning the hydrogen storage properties of Ti-V-Nb-Cr alloys by controlling the Cr/(TiVnb) ratio, *J. Alloy. Compd.* 932 (2023) 167609, <https://doi.org/10.1016/j.jallcom.2022.167609>.
- [8] B.H. Silva, W.J. Botta, G. Zepon, Design of a Ti-V-Nb-Cr alloy with room temperature hydrogen absorption/desorption reversibility, *Int. J. Hydrogen Energy* 48 (2023) 32813–32825, <https://doi.org/10.1016/j.ijhydene.2023.05.032>.
- [9] R.B. Strozi, D.R. Leiva, J. Huot, W.J. Botta, G. Zepon, An approach to design single BCC Mg-containing high entropy alloys for hydrogen storage applications, *Int. J.*

- Hydrogen Energy 46 (2021) 25555–25561, <https://doi.org/10.1016/j.ijhydene.2021.05.087>.
- [10] M.M. Nygård, G. Ek, D. Karlsson, M.H. Sørby, M. Sahlberg, B.C. Hauback, Counting electrons - a new approach to tailor the hydrogen sorption properties of high-entropy alloys, *Acta Mater.* 175 (2019) 121–129, <https://doi.org/10.1016/j.actamat.2019.06.002>.
- [11] M.M. Nygård, G. Ek, D. Karlsson, M. Sahlberg, M.H. Sørby, B.C. Hauback, Hydrogen storage in high-entropy alloys with varying degree of local lattice strain, *Int. J. Hydrogen Energy* 44 (2019) 29140–29149, <https://doi.org/10.1016/j.ijhydene.2019.03.223>.
- [12] B.H. Silva, C. Zlotea, Y. Champion, W.J. Botta, G. Zepon, Design of TiVNb-(Cr, Ni or Co) multicomponent alloys with the same valence electron concentration for hydrogen storage, *J. Alloy. Compd.* 865 (2021) 158767, <https://doi.org/10.1016/j.jallcom.2021.158767>.
- [13] O.A. Pedroso, W.J. Botta, G. Zepon, An open-source code to calculate pressure-composition-temperature diagrams of multicomponent alloys for hydrogen storage, *Int. J. Hydrogen Energy* 47 (2022) 32582–32593, <https://doi.org/10.1016/j.ijhydene.2022.07.179>.
- [14] J. Hu, H. Shen, M. Jiang, H. Gong, H. Xiao, Z. Liu, et al., A DFT study of hydrogen storage in high-entropy alloy Ti<sub>2</sub>ZrHfScMo, *Nanomaterials* 9 (2019) 1–12, <https://doi.org/10.3390/nano9030461>.
- [15] G. Zepon, B.H. Silva, C. Zlotea, W.J. Botta, Y. Champion, Thermodynamic modelling of hydrogen-multicomponent alloy systems: calculating pressure-composition-temperature diagrams, *Acta Mater.* 215 (2021) 117070, <https://doi.org/10.1016/j.actamat.2021.117070>.
- [16] G. Andrade, B.H. Silva, G. Zepon, R. Floriano, Hydrogen storage properties of Zr-based multicomponent alloys with C14-Laves phase structure derived from the Zr–Cr–Mn–Fe–Ni system, *Int. J. Hydrogen Energy* 51 (2024) 246–254, <https://doi.org/10.1016/j.ijhydene.2023.11.111>.
- [17] J.B. Ponsoni, V. Aranda, T. da S. Nascimento, R.B. Strozi, W.J. Botta, G. Zepon, Design of multicomponent alloys with C14 laves phase structure for hydrogen storage assisted by computational thermodynamic, *Acta Mater.* 240 (2022), <https://doi.org/10.1016/j.actamat.2022.118317>.
- [18] J.B. Ponsoni, M. Balcerzak, W.J. Botta, M. Felderhoff, G. Zepon, A comprehensive investigation of the (Ti<sub>0.5</sub>Zr<sub>0.5</sub>)<sub>1</sub>(Fe<sub>0.33</sub>Mn<sub>0.33</sub>Cr<sub>0.33</sub>)<sub>2</sub> multicomponent alloy for room-temperature hydrogen storage designed by computational thermodynamic tools, *J. Mater. Chem. A Mater.* 11 (2023) 14108–14118, <https://doi.org/10.1039/d3ta02197a>.
- [19] G. Zepon, D.R. Leiva, R.B. Strozi, A. Bedoch, S.J.A. Figueiroa, T.T. Ishikawa, et al., Hydrogen-induced phase transition of MgZrTiFe0.5Co<sub>0.5</sub>Ni<sub>0.5</sub> high entropy alloy, *Int. J. Hydrogen Energy* 43 (2018) 1702–1708, <https://doi.org/10.1016/j.ijhydene.2017.11.106>.
- [20] M. Sahlberg, D. Karlsson, C. Zlotea, U. Jansson, Superior hydrogen storage in high entropy alloys, *Sci. Rep.* 6 (2016) 1–6, <https://doi.org/10.1038/srep36770>.
- [21] D. Karlsson, G. Ek, J. Cedervall, C. Zlotea, K.T. Møller, T.C. Hansen, et al., Structure and hydrogenation properties of a HfNbTiVzr high-entropy alloy, *Inorg. Chem.* 57 (2018) 2103–2110, <https://doi.org/10.1021/acs.inorgchem.7b03004>.
- [22] P. Edalati, R. Floriano, A. Mohammadi, Y. Li, G. Zepon, H.W. Li, et al., Reversible room temperature hydrogen storage in high-entropy alloy Ti<sub>2</sub>ZrCrMnFeNi, *Scr. Mater.* 178 (2020) 387–390, <https://doi.org/10.1016/j.scriptamat.2019.12.009>.
- [23] R. Floriano, G. Zepon, K. Edalati, G.L.B.G. Fontana, A. Mohammadi, Z. Ma, et al., Hydrogen storage in Ti<sub>2</sub>ZrNbFeNi high entropy alloys, designed by thermodynamic calculations, *Int. J. Hydrogen Energy* 45 (2020) 33759–33770, <https://doi.org/10.1016/j.ijhydene.2020.09.047>.
- [24] J. Montero, G. Ek, L. Laversenne, V. Nassif, G. Zepon, M. Sahlberg, et al., Hydrogen storage properties of the refractory Ti–V–Zr–Nb–Ta multi-principal element alloy, *J. Alloy. Compd.* 835 (2020) 155376, <https://doi.org/10.1016/j.jallcom.2020.155376>.
- [25] V. Aranda, D.R. Leiva, J. Huot, W.J. Botta, G. Zepon, Hydrogen storage properties of the Ti<sub>2</sub>VFeZr multicomponent alloy with C14-type laves phase structure, *Intermet. (Barking)* 162 (2023), <https://doi.org/10.1016/j.intermet.2023.108020>.
- [26] L.F. Chanchetti, B. Hessel Silva, J. Montero, C. Zlotea, Y. Champion, W.J. Botta, et al., Structural characterization and hydrogen storage properties of the Ti<sub>31</sub>V<sub>26</sub>Nb<sub>26</sub>Zr<sub>12</sub>M<sub>5</sub> (M = Fe, Co, or Ni) multi-phase multicomponent alloys, *Int. J. Hydrogen Energy* (2022) 8, <https://doi.org/10.1016/j.ijhydene.2022.10.060>.
- [27] S. Dangwal, K. Edalati, Significance of interphase boundaries on activation of high-entropy alloys for room-temperature hydrogen storage, *Int. J. Hydrogen Energy* 50 (2024) 626–636, <https://doi.org/10.1016/j.ijhydene.2023.07.327>.
- [28] K. Sakaki, H. Kim, K. Asano, Y. Nakamura, Hydrogen storage properties of Nb-based solid solution alloys with a BCC structure, *J. Alloy. Compd.* 820 (2020) 153399, <https://doi.org/10.1016/j.jallcom.2019.153399>.
- [29] G.C. Mayer Dias, B.H. Silva, A. de Sousa Martins, M. Felderhoff, W.J. Botta, G. Zepon, Hydride destabilization in the Ti-Nb-Cr system through Nb/Ti ratio adjustment, *ACS Appl. Energy Mater.* (2024), <https://doi.org/10.1021/acsaem.4c01167>.
- [30] B.H. Silva, C. Zlotea, G. Vaughan, Y. Champion, W.J. Botta, G. Zepon, Hydrogen absorption/desorption reactions of the (TiVNb)<sub>85</sub>Cr<sub>15</sub> multicomponent alloy, *J. Alloy. Compd.* 901 (2022) 163620, <https://doi.org/10.1016/j.jallcom.2022.163620>.
- [31] J.J. Reilly, R.H. Wiswall, Higher hydrides of vanadium and niobium, *The* 9 (1970).
- [32] B.H. Toby, R.B. Von Dreele, GSAS-II: the genesis of a modern open-source all purpose crystallography software package, *J. Appl. Crystallogr.* 46 (2013) 544–549, <https://doi.org/10.1107/S0021889813003531>.
- [33] J.C. Slater, Atomic radii in crystals, *J. Chem. Phys.* 41 (1964) 3199–3204, <https://doi.org/10.1063/1.1725697>.
- [34] G.D. Sandrock, P.D. Goodell, SURFACE POISONING OF LaNi<sub>5</sub>, FeTi AND (Fe,Mn) Ti BY O<sub>2</sub>, CO, J. Less-Common Met. 73 (1980) 161–168, [https://doi.org/10.1016/0022-5088\(80\)90355-0](https://doi.org/10.1016/0022-5088(80)90355-0).
- [35] H.Y. Zhu, J. Wu, Q.D. Wang, Reactivation behaviour of TiFe hydride, *J. Alloy. Compd.* 215 (1994) 91–95, [https://doi.org/10.1016/0925-8388\(94\)90823-0](https://doi.org/10.1016/0925-8388(94)90823-0).
- [36] C. Suryanarayana, Nanocrystalline materials, *Int. Mater. Rev.* 40 (1995) 41–64.
- [37] C. Suryanarayana, Mechanical alloying and milling, *Prog. Mater. Sci.* 46 (2001) 1–184, [https://doi.org/10.1016/S0079-6425\(99\)00010-9](https://doi.org/10.1016/S0079-6425(99)00010-9).
- [38] A. Zaluska, L. Zaluski, J.O. Ström-Olsen, Nanocrystalline magnesium for hydrogen storage, *J. Alloy. Compd.* 288 (1999) 217–225, [https://doi.org/10.1016/S0925-8388\(99\)00073-0](https://doi.org/10.1016/S0925-8388(99)00073-0).
- [39] L. Zaluski, A. Zaluska, P. Tessier, J.O. Ström-Olsen, R. Schulz, Catalytic effect of Pd on hydrogen absorption in mechanically alloyed Mg<sub>2</sub>Ni, LaNi<sub>5</sub> and FeTi, *J. Alloy. Compd.* 217 (1995) 295–300, [https://doi.org/10.1016/0925-8388\(94\)01358-6](https://doi.org/10.1016/0925-8388(94)01358-6).
- [40] C. Zhang, Y. Wu, L. You, X. Cao, Z. Lu, X. Song, Investigation on the activation mechanism of hydrogen absorption in Ti<sub>2</sub>ZrNbTa high entropy alloy, *J. Alloy. Compd.* 781 (2019) 613–620, <https://doi.org/10.1016/j.jallcom.2018.12.120>.
- [41] B.H. Silva, J.M.P. Almeida, A.C. Hernandez, R.V. Gonçalves, G. Zepon, Pulsed laser activation method for hydrogen storage alloys, *Int. J. Hydrogen Energy* 53 (2024) 885–890, <https://doi.org/10.1016/j.ijhydene.2023.12.143>.
- [42] T.B. Flanagan, W.A. Oates, Some thermodynamic aspects of metal hydrogen systems, *J. Alloy. Compd.* 404–406 (2005) 16–23, <https://doi.org/10.1016/j.jallcom.2004.11.108>.
- [43] T.B. Flanagan, J.D. Clewley, Hysteresis in metal hydrides, *J. Less-Common Met.* 83 (1982) 127–141, [https://doi.org/10.1016/0022-5088\(82\)90176-X](https://doi.org/10.1016/0022-5088(82)90176-X).
- [44] J. Zhang, P. Li, G. Huang, W. Zhang, J. Hu, H. Xiao, et al., Superior hydrogen sorption kinetics of Ti 0.20 Zr 0.20 Hf 0.20 Nb 0.40 high-entropy alloy, *Metals* 11 (2021) 470, <https://doi.org/10.3390/met>.
- [45] L. Hao, C. Yungui, Y. Yigang, W. Chaoling, T. Mingda, Cyclic properties of hydrogen absorption and desorption in V-Ti-Cr-Fe(Al,Si) alloy, *Mater. Sci. Eng. A* 448 (2007) 128–134, <https://doi.org/10.1016/j.msea.2006.10.055>.
- [46] J. Montero, C. Zlotea, G. Ek, J. Crivello, L. Laversenne, M. Sahlberg, Ti<sub>2</sub>ZrNb multi-principal-element alloy: sorption properties, *Molecules* 24 (2019) 1–14.
- [47] A. Kumar, K. Shashikala, S. Banerjee, J. Nuwad, P. Das, C.G.S. Pillai, Effect of cycling on hydrogen storage properties of Ti 2CrV alloy, *Int. J. Hydrogen Energy* 37 (2012) 3677–3682, <https://doi.org/10.1016/j.ijhydene.2011.04.135>.
- [48] R.B. Strozi, M. Witman, V. Stavila, J. Cizek, K. Sakaki, H. Kim, et al., Elucidating primary degradation mechanisms in high-cycling-capacity, compositionally tunable high-entropy hydrides, *ACS Appl. Mater. Interfaces* 15 (2023) 38412–38422, <https://doi.org/10.1021/acsami.3c05206>.